MICROFOCUS COMPUTED X-RAY TOMOGRAPHY OF SEGREGATIONS IN HIGH STRENGTH ALUMINIUM ALLOYS

Bernhard HARRER*,**, H. Peter DEGISCHER**, Johann KASTNER*
* Upper Austrian University of Applied Sciences, Wels Campus, 4600, Austria
** Institute of Materials Science and Technology, University of Technology Vienna, 1040, Austria

Abstract

On the basis of selected examples of Al-Cu-Mg and Al-Zn-Mg-Cu alloys, the possibilities and limits of high–resolution cone–beam microfocus X-ray computed tomography with a transmission target (μXCT) yielding a minimum voxel size of $(1\ \mu m)^3$ will be presented. Alignments and the formation of the dendritic structure are shown in 3D. Thereby important additional information and a better understanding of the casting process can be achieved.

Furthermore we show a method for the differentiation of different types of segregations (interdendrititc eutectic and $Al_3(Sc,Zr)$ dispersoids), which both appear higher-absorbing in comparison to the Al–matrix. The microstructures have been verified using metallographic techniques.

1. Introduction

High strength wrought aluminium alloys are widely used in aerospace vehicles because of their high specific stiffness and strength, good hot workability and resistance to corrosion. The as–cast microstructure of the pre-material for rolling, extrusion and forging, basically consists of α-Al dendrites and interdendritic eutectic regions due to segregations. Sc and Zr are added to aluminium alloys to form $Al_3(Sc,Zr)$ dispersoids; these dispersoids serve to activate grain nucleation and inhibit grain growth, resulting in improved strength and toughness [1].

Due to measurement-speed and quality, XCT-systems with cone beam geometry and 2D matrix detectors have gained a general acceptance in materials science as well as in industry [2, 3]. When using cone-beam XCT, a specimen is placed on a rotary stage between the X-ray source and the detector. The specimen is rotated step by step, taking a projection image at each angular position. A computer cluster reconstructs the projections to a volume dataset. A grey value is calculated for each position of the resulting dataset (i.e. a volume element called voxel) in the scanned sample volume. The determined grey values correspond to the effective X-ray attenuation coefficient μ which is a function of the density and the atomic number of the elements within that voxel (x,y,z).

2. Experimental

2.1 Samples

Samples from an AlCu4Mg1 and two Al-Zn-Mg-Cu continously cast slabs and billets, respectively, were investigated; a summary of these samples can be found in Table 1. The position of sampling within the Al-slabs was the following: Sample A was taken from the center of the as-cast slab of 300 mm width. The two Al-Zn-Mg-Cu samples B and C were taken from the outer surface of an as-cast billet [4, 5].

Table 1. Description of the investigated Al-Cu-Mg and Al-Zn-Mg-Cu samples.

Sample	Alloy	Concentration of main elements (weight %)	Sample`s cross section (mm^2)	Production state
A	AlCu4Mg1 (EN AW-2024)	4 % Cu, 1 % Mg	3,5 × 5,0	As-cast slabs
B	AlZn8Mg2Cu2 (EN AW-7349)	7,7% Zn; 2,3% Mg; 1,5% Cu; 0,11% Zr; 0,25% Sc	2,2 × 2,5	As-cast billet
C	AlZn6Mg2Cu2 (EN AW-7010)	6,4% Zn; 2,2% Mg; 1,7% Cu; 0,11% Zr; 0,26% Sc	0,7 × 1,2	As-cast billet

2.2. Computed Tomography

- CT-data recording

  The X-ray tomograms were scanned using a *nanotom 180NF CT* device constructed by *GE Sensing & Inspection Technologies* Inc. with a 180 keV nanofocus transmission tube and a 2316 × 2316 pixel *Hamamatsu* detector. The minimal spot size in that device is > 0.8 µm. Further details can be found in [6, 7]. The target used for generating photons was made of tungsten. Table 2 gives an overview of the most important CT-measurement parameters. These parameters have lead to measurement-times between 120 and 200 min per scan.

- CT-data evaluation

  The cone beam XCT-data were reconstructed by a filtered back projection Feldkamp-algorithm [8]. A beam hardening correction, a ring artefact correction and a calibration of the center of rotation was performed for all XCT-data [7]. The reconstructed data were processed and visualised with the program *VGStudio MAX 2.0,* which provides not only global thresholds for the whole dataset but also local thresholds for parts of the measurement-volumes are applicable. Segmentations were performed using these grey value thresholds and special region growing-algorithms [9].

  The shape factor F (sphericity) was used according to equ. (1) to differentiate segmented heterogeneities with different three-dimensional shapes [10].

$$F = 6\sqrt{\pi}\,\frac{volume}{\sqrt{surface^3}} \qquad \text{where } F \in [0, 1], \text{ ideal sphere } F = 1 \qquad (1)$$

2.3. Metallographic analysis for verification of the CT-results

To identify the different heterogeneities and phases, selected regions of the samples were investigated by means of metallographic analysis and scanning electron microscopy (SEM). The elemental analysis was carried out by energy dispersive X-ray analysis (EDX) [11]. Further details can be found in [5, 12].

Table 2. Overview of the most important measurement parameters.

Sample	Acceleration voltage (kV)	Beam current (µA)	Number of projections	Integration time (s)	Pre-filter inserted	Voxel size $(\mu m)^3$
A	100	135	1400	0,5	0,1 mm Cu	$(1,1)^3$
B	100	115	2000	0,5	none	$(2,3)^3$
C	80	100	1800	0,5	none	$(1,5)^3$

3. Results and Discussion

3.1 AlCu4Mg1 slabs

Figure 1 shows the result of the CT–measurement of sample A with a voxel size of $(1.1\ \mu m)^3$. The higher-absorbing interdendritic Al-Al_2Cu-eutectic appears brighter than the Al–dendrites. In addition to the phases, some micropores with diameters between 4–13 µm could be found. It is possible to segment the highly absorbing interdendritic regions and to measure their thickness down to a width of approx. 4 µm. The structure of the complementary α-Al dendrite arms with a diameter between 50–100 µm can be identified in Figure 1 (c) and (d).

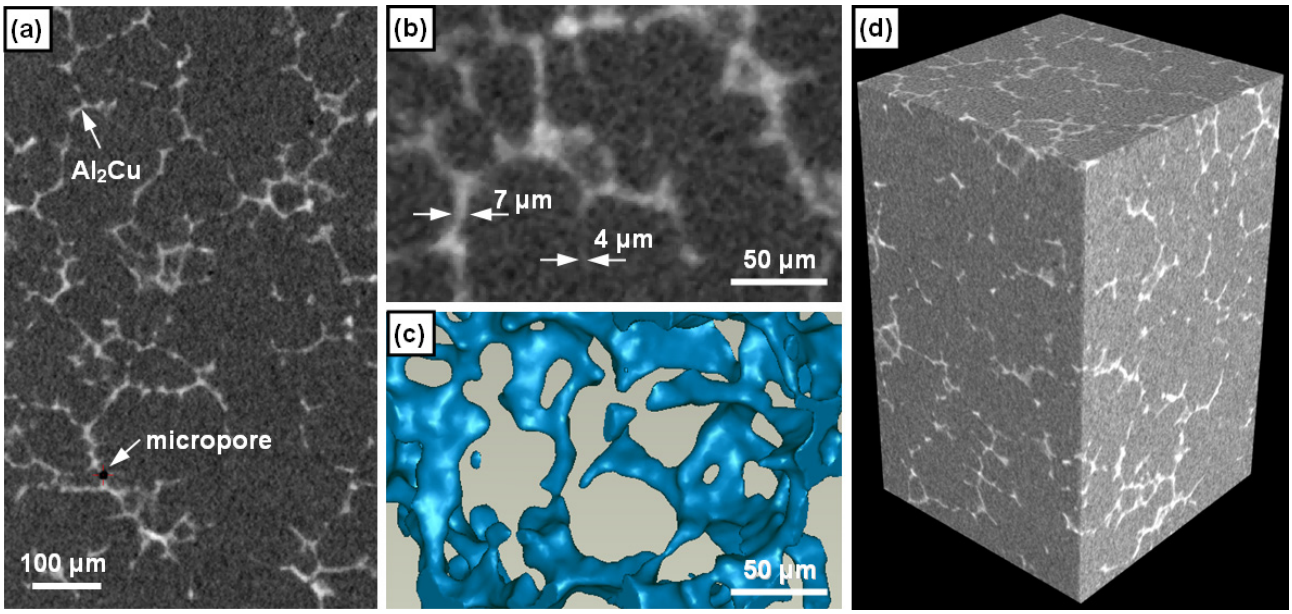

Figure 1: High-resolution µXCT and segmentations of eutectic Al-Al_2Cu regions in sample A: (a) cross section with bright interdendritic eutectic and a micropore; (b) enlarged cross section and measured thickness of interdendritic space; (c) connectivity of the segmented eutectic regions, (d) 550 × 550 × 850 μm^3 cuboid with 3 cross sections.

For an exact identification of the interdendritic phases sample A was investigated by SEM. Figure 2 shows a cross section and an energy dispersive X-ray analysis (EDX) was accomplished for the elements Al, Cu, Mg, Fe and Mn within the range B1. As a result, most phases could be identified as Al_2Cu and $Al_xCu_yMg_z$ [12]. In addition to these eutectic phases, Fe-Mn-aluminates and Fe-Mn-Cu- aluminates appeared in some areas distinguished by EDX and the grey level in backscattered electron images (BSE).

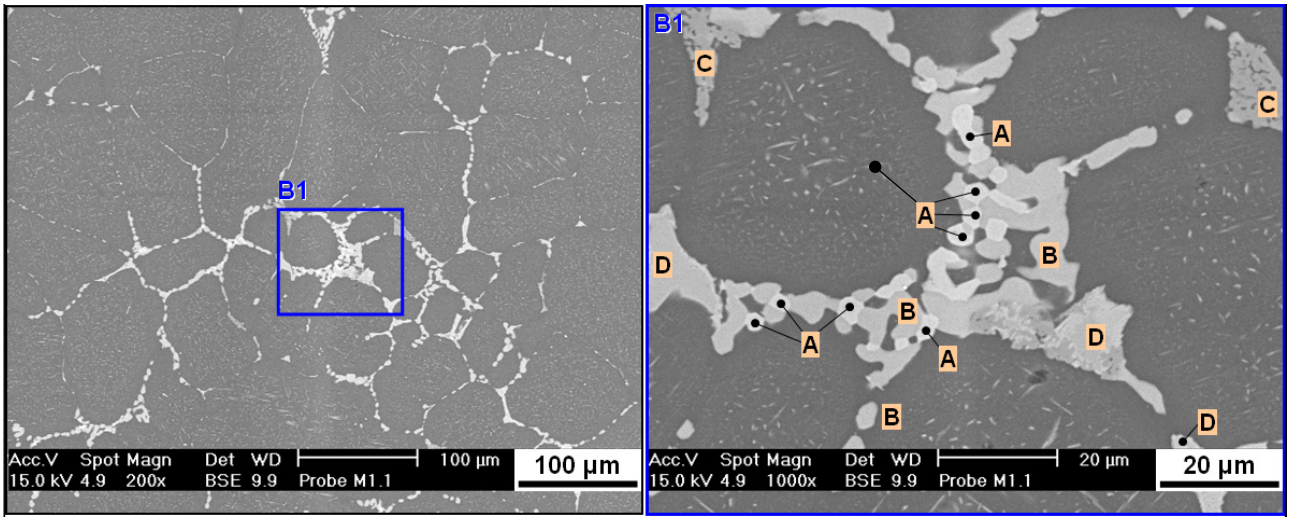

Figure 2: SEM-BSE recordings of sample A with identified phases in the enlarged area B1: Al_2Cu (A), $Al_xCu_yMg_z$ (B), Fe-Mn-aluminates (C) and Fe-Mn-Cu- aluminates (D).

3.2 Al-Zn-Mg-Cu-billets

The chill cast Al-Zn-Mg-Cu–billets (Sample B and C) contain Sc and Zr, which form mainly secondary $Al_3(Sc,Zr)$ dispersoids inhibiting grain growth, but primary $Al_3(Sc,Zr)$ may segregate as well. In addition to these particles, interdendritic segregations rich in highly absorbing elements like Zn and Cu appear.

In Figure 3 pores, segregations and a highly absorbing area at the outer edge of the slab with a width of approx. 0.45 mm could be identified in the tomograms of Sample B. Zn and Cu are distributed more homogenously in that region, than in the rest of the sample. Consequently, it can be assumed that "very fine" grains with relatively high solid solution of the alloying elements are solidified close to the surface. Segmentations of the pores and the interdendritic segregations from the α-Al dendrites are shown in a cuboid of $1.2 \times 1.3 \times 2.8$ mm^3 in Figure 3 (b) and (c).

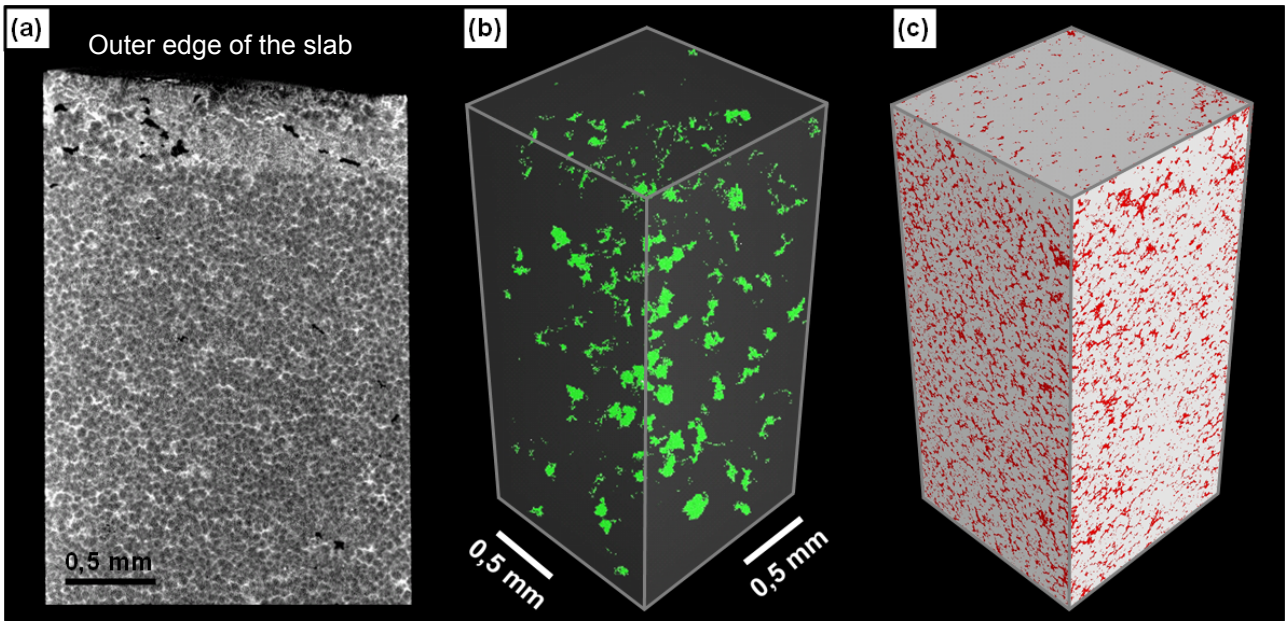

Figure 3: Tomogram and differentiation of lowly absorbing pores and highly absorbing segregations from the α-Al dendrites of sample B: (a) tomogram with highly absorbing outer edge of the slab interdendritic segregations (bright) and pores (black); (b) segmentation of the pores in a transparent volume and (c) 3 cross sections of the interdendritic segregations in the same cuboid of $1.2 \times 1.3 \times 2.8$ mm^3.

In order to detect the secondary $Al_3(Sc,Zr)$ dispersoids with higher accuracy, a smaller sample C was investigated with a voxel size of $(1{,}5\ \mu m)^3$. Figure 4 (a) shows three different types of heterogeneities:

- Low absorbing interdendritic heterogeneities with an irregular shape (pores); e.g. area B1 in Figure 4 (b).
- Highly absorbing interdendritic cell shaped structures (eutectic region of interdendritic segregations containing Zn and Cu); e.g. area B2 in Figure 4 (b).
- Highly absorbing globular (in some cases cuboidal) shaped heterogeneities and agglomerates identified as $Al_3(Sc,Zr)$–particles. These heterogeneities are mostly located in the center of cell shaped structures and Figure 4 (c) shows the smallest detected $Al_3(Sc,Zr)$–particle with a diameters of approx. 5 µm. The particle in Figure 4 (d) illustrates the cuboidal shape and is the biggest particle (approx. 50 µm) which could be detected in the investigated volume. Typical diameters of such particles are in the range of 10-20 µm.

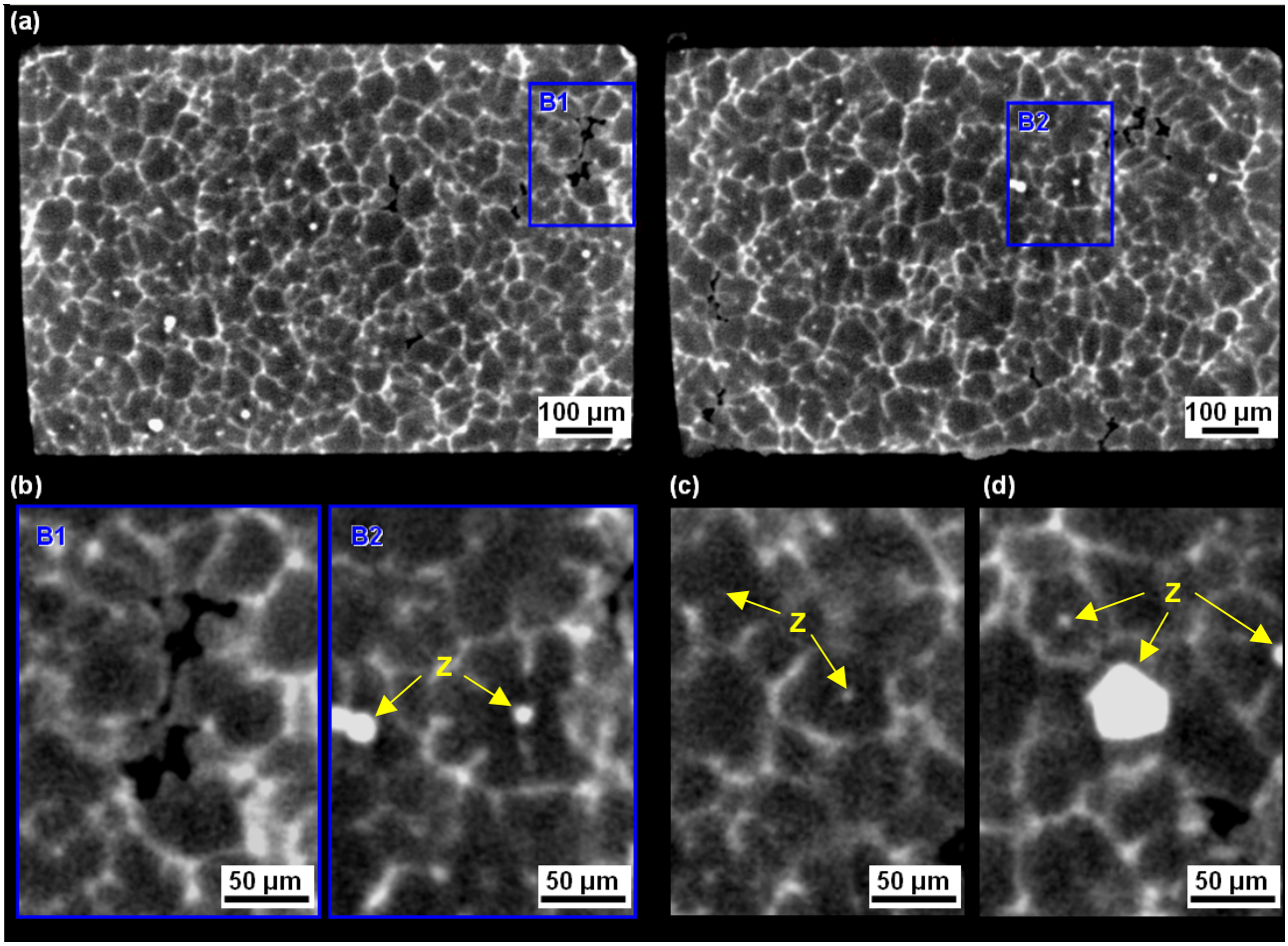

Figure 4: Slices of tomograms with different types of heterogeneities in sample C: (a) different cross sections of the sample with interdendritic segregations (bright) and white particles; (b) enlarged areas B1 with interdendritic pores and B2 with highly absorbing $Al_3(Sc,Zr)$ particles (Z); (c) smallest and (d) biggest primary $Al_3(Sc,Zr)$ detected.

Low absorbing heterogeneities have been segmented by a region growing-algorithm in a volume of 2.2 mm^3. The segmentation of pores is shown in Figure 5 (b) and their measured volume fraction is about 0.3 vol%. Due to the alignment of the principal axis of these pores the direction of solidification of the α-Al dendrites is traceable and averages at around 45° with respect to the surface of the billet.

To distinguish the highly absorbing heterogeneities (eutectic region and $Al_3(Sc,Zr)$-particles) from the α-Al dendrites the image quality was good enough in order to use local thresholds (ISO-thresholds). The results of that segmentation are shown in Figure 5 (c). A volume fraction of 16–17 vol% of highly absorbing regions could be estimated.

Both, the eutectic region and the $Al_3(Sc,Zr)$-particles are similarly absorbing more X-rays than the α-Al dendrites. Because of the limited spatial resolution and the appearance of physical artefacts, it was not possible to differentiate between these two types of heterogeneities by means of the contrast level. Since the $Al_3(Sc,Zr)$–particles exhibit more or less equi-axial shapes, it is feasible to separate them from the irregular eutectic by means of a shape factor. Thus, the shape factor F which describes the three-dimensional sphericity of each individual heterogeneity was introduced (see equ. 1). The results of applying F on the volume B3 (Figure 5a), is illustrated in Figure 6 (a): A suitable threshold of $F = 0.4$ was found and 190 almost spherical $Al_3(Sc,Zr)$–particles could be distinguished from the eutectic region in this volume of $1.09 \times 0.73 \times 0.14$ mm^3. The volume fraction of the $Al_3(Sc,Zr)$–particles amounts 0,17 vol%, their number density is > 1500/mm^3 and they are centered within dendrites.

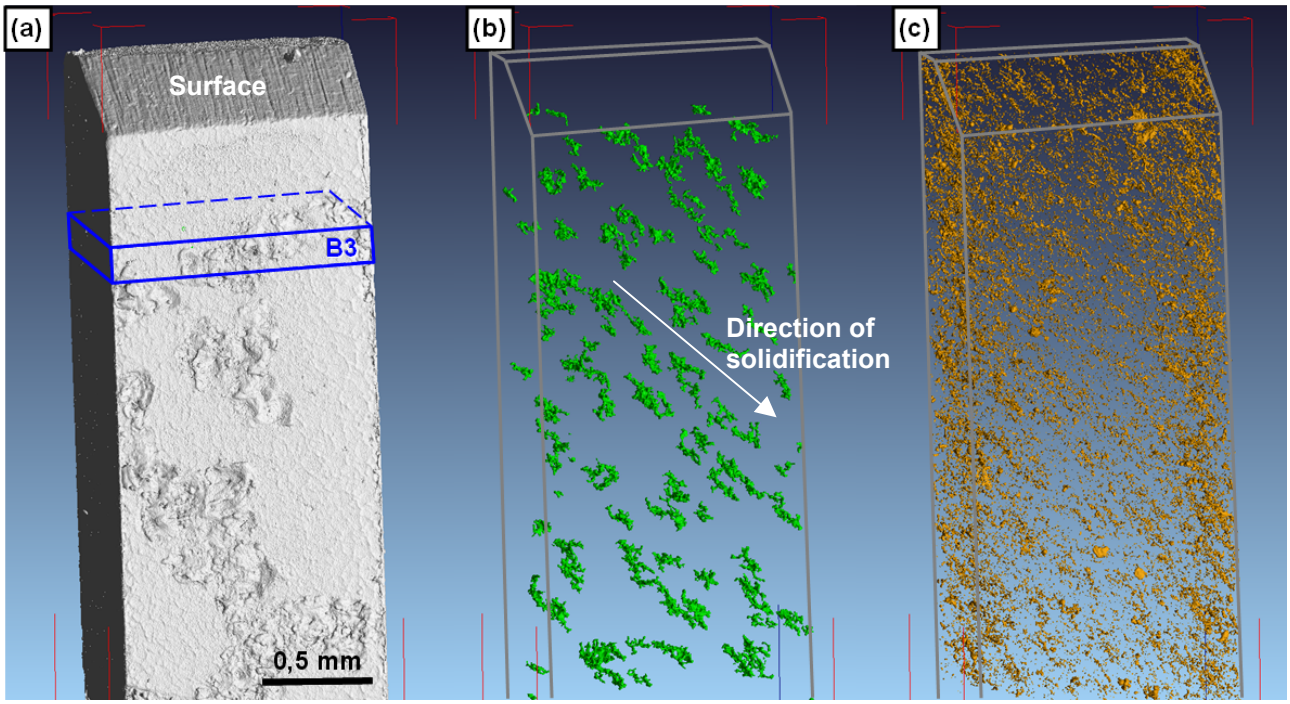

Figure 5: 3D illustrations of segmentations in sample C: (a) surface near region with marked volume B3; (b) pores in the direction of solidification; (c) eutectic region and $Al_3(Sc,Zr)$–particles.

Figure 7 (a) shows three orthogonal tomogram slices of an α-Al dendrite (white). The interdendritic eutectic region and an $Al_3(Sc,Zr)$–particle located in the center of the dendrites were faded out. The diameter of the star-shaped dendrite is about 190 µm whereby the arms width reaches up to 30 µm. Figure 7 (c) and (d) illustrate further typical arrangements of α-Al dendrites with a size of about 130 µm, centrally placed $Al_3(Sc,Zr)$–particles and eutectic regions between. In Figure 7 (d) a bigger volume of $0.27 \times 0.29 \times 0.12$ mm^3 with several dendritic structures with a diameter up to 120 µm is imaged with centrally placed $Al_3(Sc,Zr)$–particles.

The position of the several µm big equi axial $Al_3(Sc,Zr)$–particles indicates that they act as seed crystals for the α-Al dendrites and are segregated primarily from the melt.

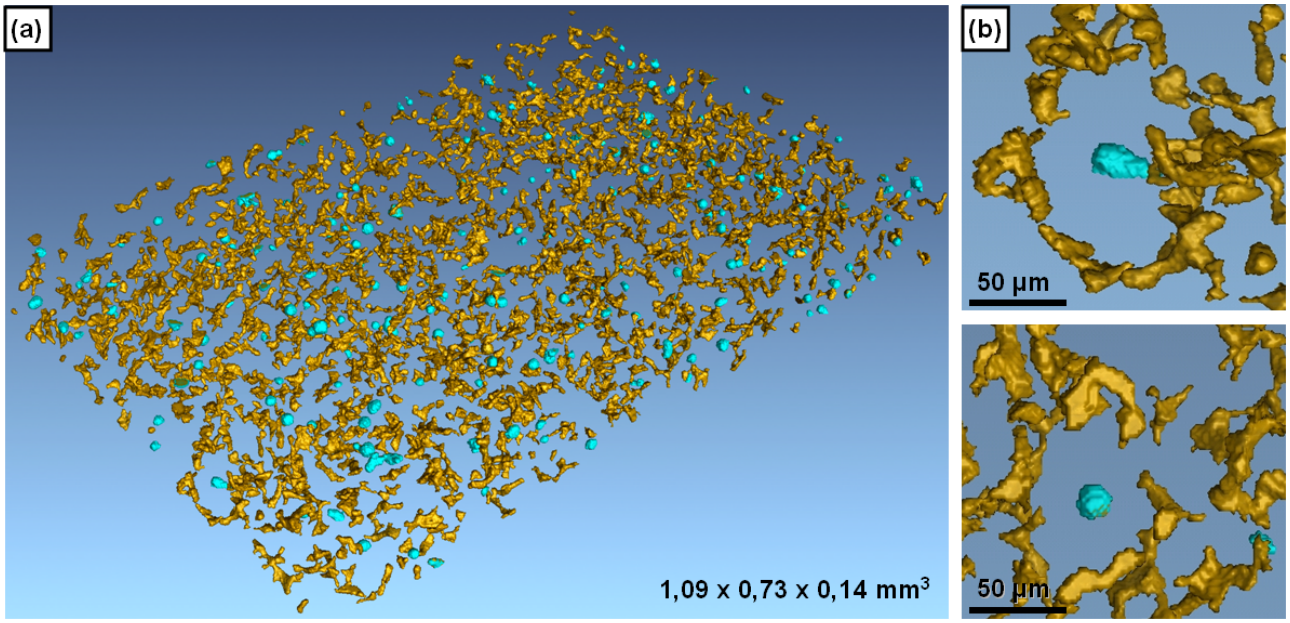

Figure 6: Differentiation between $Al_3(Sc,Zr)$–particles (turquoise) from the eutectic region (gold): (a) 3D view of volume B3 from Figure 5 (a); (b) enlarged pictures where $Al_3(Sc,Zr)$–particles are located centrally in the α-Al dendrites.

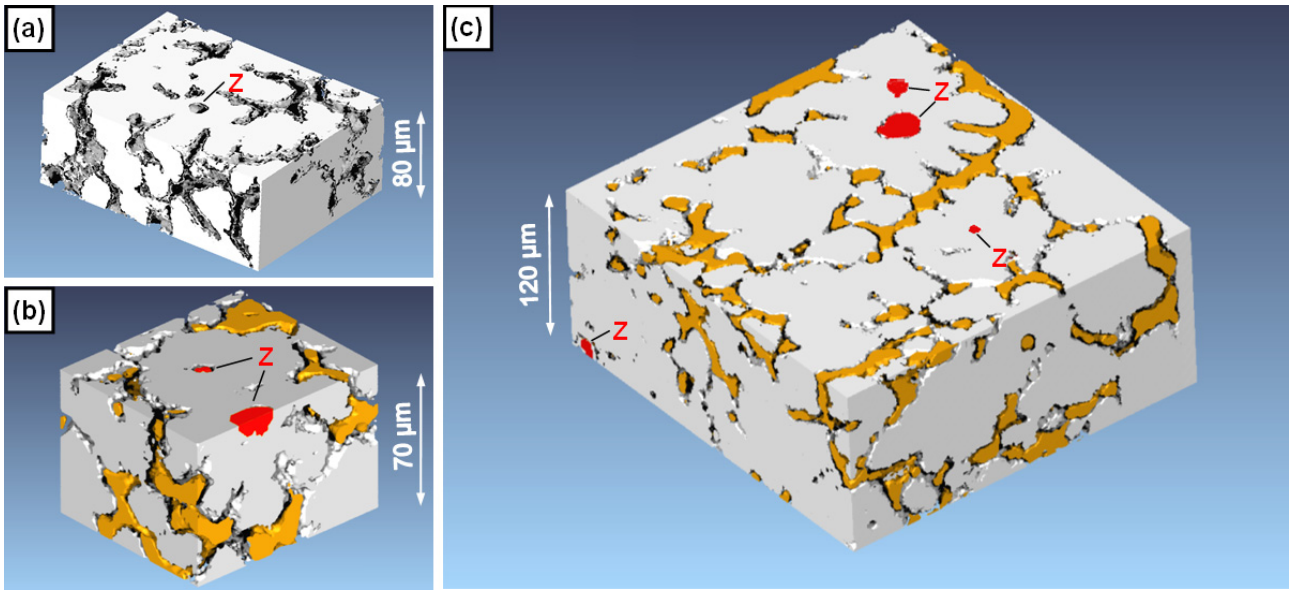

Figure 7: Typical arrangements of α-Al dendrites (white), interdendritic eutectic regions (orange) and $Al_3(Sc,Zr)$–particles (Z) in sample C: (a) α-Al dendrite in a cuboid of 0,21 × 0,15 × 0,08 mm^3; (b) cuboid with a volume of 0,09 × 0,11 × 0,07 mm^3 and (e) 0,27 × 0,29 × 0,12 mm^3.

The light-optical recordings and energy dispersive X-ray analysis (EDX) show in Figure 8 that the eutectic region is composed of Zn_2Mg and Cu-rich phases [11]. In addition $Al_3(Sc, Zr)$-particles < 50 µm in diameter mainly in the center of α-Al dendrites and interdendritic pores with a width up to 100 µm appear.

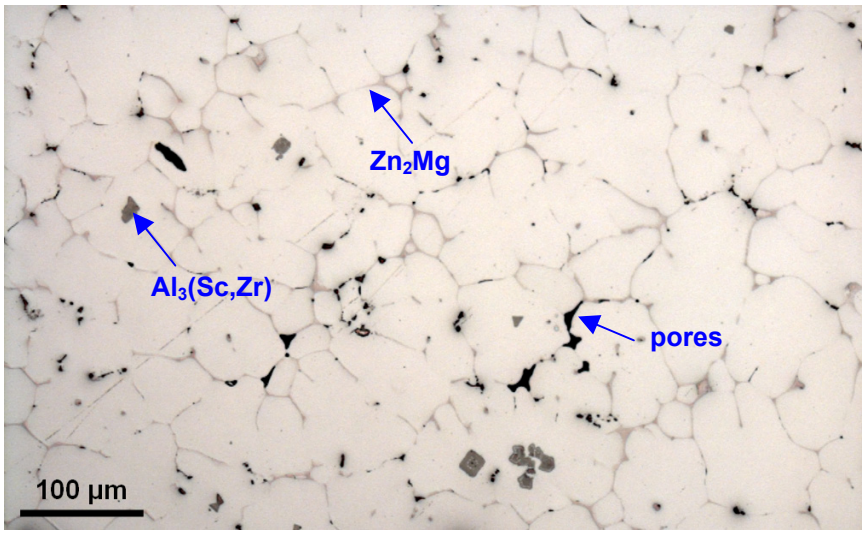

Figure 8: Light optical microscope image of a cross section of sample C and the interpretation of the phases: $Al_3(Sc, Zr)$-particles displayed in grey mainly located in the center of the α-Al dendrites (white), interdendritic Zn_2Mg and Cu-rich phases (grey) and pores (black).

4. Conclusion

- Apart from the detection of interdendritic shrinkage pores, it is possible to quantify the eutectic segregations and primary $Al_3(Sc,Zr)$–particles bigger than 50 $µm^3$ in as–cast Zn and/or Cu containing high strength aluminium alloys by high-resolution µXCT in 3D.
- The morphology and distribution of the interdendritic eutectic replicates the dendritic solidification structure, where the orientation and width of the individual dendrite arms can be measured. Conclusions on the speed and direction of the solidification process can be drawn from those results at different positions in the slab.

- The morphology and the extension of the interdendritic segregations can be determined in 3D with high accuracy in different positions of a casting within a relatively big volume (in comparison to 2D metallographic techniques).
- The ability to differentiate between globular $Al_3(Sc,Zr)$–particles and the complex interdendritic segregations of elements heavier than Al allows the estimation of the amount of primary $Al_3(Sc,Zr)$–particles bigger than 5 µm. The metallurgist deduces the amount of primary $Al_3(Sc,Zr)$ and their function as solidification seeds.
- To a large extent there is a linear connection between the detectability of heterogeneities and the voxel size. It is possible to identify the studied heterogeneities in aluminium alloys with a diameter of at least 3-5 voxel for reliable detection (i.e. a volume > 30 voxels).

Acknowledgement
The authors gratefully acknowledge: the provision of samples by the company AMAG rolling GmbH and Honsel; SEM- and metallographic investigations by H. Knoblich and Z. Asghar of the University of Technology Vienna. The project was supported by the COMET program of the FFG and the Austrian research funds FWF.

[1] J. R. Davis (Editor): *Aluminum and Aluminum Alloys (Asm Specialty Handbook),* ASM International, 1993, ISBN-10: 087170496X.
[2] J. Baruchel, J. Y. Buffière, E. Maire, G. Peix (Editors), *X-ray tomography in material science*, Paris: Hermes Science Publication; 2000.
[3] J. Kastner (Editor): *Proceedings Industrielle Computertomografietagung*, Wels, Austria, February 2008, Aachen: Shaker Verlag; 2008.
[4] R. Schneider: *Weldability of high-strength aluminium alloys for aerospace applications.* PhD thesis, University of Technology Vienna, Institute of Materials Science and Technology, 2008.
[5] B. Harrer: *Detektierbarkeit von Heterogenitäten in Fe-Basis- und Aluminiumlegierungen mittels Röntgen- Computertomographie*; PhD thesis, University of Technology Vienna, Institute of Materials Science and Technology, 2009.
[6] O. Brunke, K. Brockdorf, S. Drews, B. Müller, T. Donath, J. Herzen, F. Beckmann: *Comparison between X-ray tube based and synchrotron radiation based µCT*, Development in X-ray tomography VI, S.R. Stock (Editor), Proceedings of SPIE 2008, 7078: 1-12.
[7] phoenix|x-ray (Editor): *Manual: nanotom 180NF*. Online http://www.phoenix-xray.com/de/index.php [28.06.2009].
[8] L.A. Feldkamp, L.C. Davis, J.W. Kress: *Practical cone beam algorithm.* In: Journal of the Optical Society of America 1, 1984, 6, 612-619.
[9] Volume Graphics GmbH (Editor): *Reference Manual VGStudio Max Release 2.0*, Online: http://www.volumegraphics.com [28.03.2009].
[10] F. Mücklich, J. Ohser: *Statistical Analysis of Microstructures in Materials Science*. Weinheim, Wiley and Sons, 2000, ISBN-10 0471974862.
[11] Z. Asghar, C. Zaruba, University of Technology Vienna, internal report, Institute of Materials Science and Technology, 2007.
[12] L.F. Mondolfo: *Aluminium Alloys: Structure and Properties*. Butterworths, 1976.